

Nitrogen as the best interstitial dopant among $X=B, C, N, O$ and F for strong permanent magnet $NdFe_{11}TiX$: First-principles study

Yosuke Harashima,^{1,3} Kiyoyuki Terakura,^{1,4} Hiori Kino,^{2,3} Shoji Ishibashi,¹ and Takashi Miyake^{1,3}

¹*Nanomaterials Research Institute, AIST, Tsukuba, Ibaraki 305-8568, Japan*

²*MANA, National Institute for Materials Science, Tsukuba, Ibaraki 305-0044, Japan*

³*ESICMM, National Institute for Materials Science, Tsukuba, Ibaraki 305-0047, Japan*

⁴*National Institute for Materials Science, Tsukuba, Ibaraki 305-0047, Japan*

(Dated: May 8, 2019)

We study magnetic properties of $NdFe_{11}TiX$, where $X=B, C, N, O$, and F , by using first-principles calculations based on density functional theory. Its parent compound $NdFe_{11}Ti$ has the $ThMn_{12}$ structure, which has the symmetry of space group $I4/mmm$, No. 139. The magnetization increases by doping B, C, N, O , and F at the $2b$ site of the $ThMn_{12}$ structure. The amount of the increase is larger for $X=N, O, F$ than for $X=B, C$. On the other hand, the crystal field parameter $\langle r^2 \rangle A_2^0$, which controls the axial magnetic anisotropy of the $Nd\ 4f$ magnetic moment, depends differently on the dopant. With increase of the atomic number from $X=B$, $\langle r^2 \rangle A_2^0$ increases, takes a maximum value for $X=N$, and then turns to decrease. This suggests that in $NdFe_{11}TiX$, nitrogen is the most appropriate dopant among B, C, N, O , and F for permanent magnets in terms of magnetization and anisotropy. The above calculated properties are explained based on the detailed analysis of the electronic structures of $NdFe_{11}TiX$.

I. INTRODUCTION

Large remanent magnetization and high coercivity are the two fundamental requirements for high performance permanent magnets. The remanent magnetization is determined by spontaneous spin and orbital moments of a material. The coercivity is strongly correlated to the magnetocrystalline anisotropy energy. Extensive studies have been devoted to the search for higher-performance permanent magnets. The strongest permanent magnet to date is based on $Nd_2Fe_{14}B$, which has magnetization of 1.85 T at 4.2 K, magnetocrystalline anisotropy field of 67 kOe at room temperature, and Curie temperature of 586 K.¹ $NdFe_{11}TiN$ (Fig. 1) is also a strong magnet compound, although its maximum energy product is smaller than $Nd_2Fe_{14}B$. The interstitial-nitrogenated $NdFe_{11}Ti$ has magnetization of 1.476 T at 1.5 K, magnetocrystalline anisotropy field of 80 kOe at room temperature, and Curie temperature of 740 K.^{2,3}

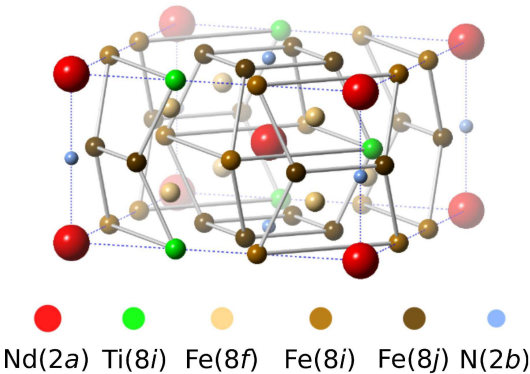


FIG. 1. (Color online) Crystal structure of $NdFe_{11}TiN$. Ti occupies one of the $8i$ sites.

$NdFe_{11}Ti$ has the $ThMn_{12}$ structure (space group $I4/mmm$, No. 139). Ideally all of the Mn sites are occupied by Fe. However, $NdFe_{12}$ is thermodynamically unstable, and some of Fe have to be substituted by another element to stabilize the bulk phase ($NdFe_{12-x}M_x$). For example, Ti, V, Cr, Mn, Mo, W, Al, and Si are known to serve as such substitutional elements M .^{4,5} However, as these substitutional elements reduce the magnetization⁶, the concentration of the substitutional atoms should be as small as possible. The concentration range of the substitution, x , depends on the element. In this regard, titanium is a favorable element because it stabilizes the material with small x (≈ 1).

To optimize the performance of a strong magnet, we can utilize even another degree of freedom, i.e., the interstitial dopant. In fact, magnetic properties of $NdFe_{12-x}M_x$ are significantly controlled by interstitial doping of a typical element. It is experimentally observed that the interstitial nitrogenation enhances the magnetic moment from 21.273 ($NdFe_{11}Ti$) to 23.218 $\mu_B/f.u.$ ($NdFe_{11}TiN_{0.5}$).² The Curie temperature (T_C) also rises from 570 K in $NdFe_{11}Ti$ to 740 K in its nitride.^{2,3} Furthermore, strong uniaxial magnetocrystalline anisotropy is induced by the nitrogenation.^{2,3,7} Another possible interstitial dopant is carbon.⁸⁻¹⁰ Carbon doping at an interstitial site leads to increase of T_C and uniaxial anisotropy in $NdFe_{12-x}M_x$ compounds. However, nitrogenation is more preferable than carbonation in terms of magnetization and Curie temperature. In order to design better strong magnets, the cause of the difference between N and C has to be clarified and the possibility of better dopants has to be searched for.

In previous papers,^{11,12} we have theoretically studied the effects of Ti substitution and nitrogenation by comparing $NdFe_{12}$, $NdFe_{11}Ti$ and $NdFe_{11}TiN$ using experimental structures. We found that Ti substitution in $NdFe_{12}$ reduces the magnetic moment more than sub-

tracting the local magnetic moment at the substituted Fe site, and enhances the uniaxial anisotropy slightly. It was also shown that interstitial nitrogenation increases the magnetic moment by $2.75 \mu_B/\text{f.u.}$ in $\text{NdFe}_{11}\text{Ti}$. The magnetic anisotropy of $\text{NdFe}_{11}\text{Ti}$ and its nitride was studied by using the crystal field parameter $\langle r^2 \rangle A_2^0$. We found that the interstitial nitrogenation substantially increases $\langle r^2 \rangle A_2^0$. This implies that the uniaxial anisotropy is enhanced by the nitrogenation in $\text{NdFe}_{11}\text{Ti}$. Therefore, the interstitial nitrogenation works preferably in terms of magnetization and magnetocrystalline anisotropy.

Stimulated by our work, the experimental group tried to synthesize a new strong magnet compound NdFe_{12}N and succeeded in forming a film recently.¹³ It has been shown that the film sample has better intrinsic magnetic properties than $\text{Nd}_2\text{Fe}_{14}\text{B}$, although a bulk sample is still difficult to synthesize. This experimental work, in turn, motivated us to revisit $\text{NdFe}_{11}\text{TiN}$ and related compounds in order to search for stronger permanent magnet compounds.

In the present paper, we perform detailed electronic structure calculations for $\text{NdFe}_{11}\text{TiX}$ with X the interstitial impurity of typical elements B, C, N, O, and F. We analyze in detail the electronic structures, paying particular attention to the X -2p states. Then, based on the analysis we explain the variations in structural properties, magnetization, and magnetocrystalline anisotropy caused by the interstitial dopant X .

II. CALCULATION METHODS

The calculations are carried out by using the first principles code QMAS (Quantum Materials Simulator)¹⁴ which is based on density functional theory^{15,16} and the projector augmented-wave (PAW) method.^{17,18} For the exchange-correlation energy functional, the generalized gradient approximation (GGA) is used.¹⁹ The $8 \times 8 \times 8$ k points are sampled and the cutoff energy for the plane wave basis is set to 40.0 Ry. The lattice constants and inner coordinates are optimized. $\text{NdFe}_{11}\text{TiX}$ has 4f orbitals that are strongly localized at the Nd sites. In the present study, the f-states of Nd are treated as open-core states, in which the hybridization with other orbitals is neglected completely and the atomic physics is applied to the Nd-4f states. Following Hund's first rule, we assume that Nd has three f-electrons with the full spin polarization. The self-consistent calculation makes the 4f spins antiparallel to the Fe spins.

The orbital magnetic moment is not treated in our self-consistent calculations, but that of the Nd-4f electrons is included in the total magnetic moment as follows. We assume that the Nd-4f electrons yield the local magnetic moment of $g_J J$, where g_J is the Lande g-factor, and $J = 9/2$ is the total angular momentum for the Nd-4f electrons. (For Nd-4f electrons, $J = |L - S|$, the orbital angular momentum $L = 6$, and the spin angular momentum $S = 3/2$ are given by Hund's rules.) The to-

tal magnetic moment of the whole material is estimated by adding $g_J J = 3.273 \mu_B$ to the spin magnetic moment. This spin magnetic moment is the contribution from the valence electrons other than the Nd-4f electrons. Fe has only small spin-orbit interaction compared with Nd; thus the spin-orbit interaction on Fe is neglected.

The magnetocrystalline anisotropy energy is expressed in terms of a first-order coefficient K_1 as

$$E(\theta) \approx K_1 \sin^2 \theta, \quad (1)$$

where θ is the rotation angle of the magnetization measured from the c axis. We focus on the contribution of the rare-earth 4f electrons. It can be evaluated by the interaction energy between the 4f electrons and the surrounding crystalline electric field. Because of Hund's rules, the electron distribution of the Nd-4f states deviates significantly from the spherical symmetry. The shape of the electron density distribution is uniquely related to \mathbf{J} which is parallel to the 4f magnetic moment. The non-spherical electron density distribution couples with the crystal-electric field leading to the magnetic anisotropy. Following the crystal-field theory, K_1 can be expressed by using the crystal field parameter A_2^0 as

$$K_1 = -3J(J - \frac{1}{2})\alpha_J \langle r^2 \rangle A_2^0 n_R. \quad (2)$$

Here, α_J is the Stevens factor of the rare-earth atoms, which is determined for each rare-earth element. For Nd^{3+} , $\alpha_J = -7/1089$. n_R is the Nd concentration. We evaluate $\langle r^2 \rangle A_2^0$ by the equation

$$\langle r^l \rangle A_l^m = F_l^m \int_0^{r_c} W_l^m(r) \phi^2(r) dr. \quad (3)$$

F_l^m is a prefactor of the real spherical harmonics Z_l^m and its explicit expressions can be found in, e.g., Ref. 20. W_l^m is the effective potential at the Nd site expanded by Z_l^m . ϕ is the radial function of the Nd-4f orbital, which is obtained in GGA with the self interaction correction. In Eq. (2) it is implicitly expected that ϕ is well localized, and we neglect the contribution from a tail of ϕ in Eq. (3) by introducing a cutoff radius r_c . The cutoff radius is determined so that the volume of the sphere is equal to that of the Bader region.^{21,22} (See Fig. S1 of the Supplemental Material²³ for the actual value of the atomic sphere for each X . The atomic radius for $\text{NdFe}_{11}\text{TiX}$ is also used for $\text{NdFe}_{11}\text{TiE}_X$, which denotes $\text{NdFe}_{11}\text{Ti}$ given by removing X from $\text{NdFe}_{11}\text{TiX}$ with other atoms fixed at their positions in the structure optimized.)

III. RESULTS

From the total energy of $\text{NdFe}_{11}\text{Ti}$, we found that Ti substitution is more stable at the 8i site than the 8f and 8j sites by 0.78 and 0.51 eV/f.u., respectively, which agrees with experimental indication.^{3,24} (Even though the symmetry of the ThMn_{12} structure is broken by the

TABLE I. Optimized lattice constants of NdFe₁₁TiX in units of Å. Due to Ti substitution, the system is no longer tetragonal but orthorhombic ($a \neq b$).

	a	b	c	volume
$X=B$	8.521	8.593	4.943	180.9
C	8.495	8.572	4.914	178.9
N	8.537	8.618	4.880	179.5
O	8.658	8.704	4.786	180.3
F	8.812	8.830	4.745	184.6
empty	8.553	8.568	4.701	172.3

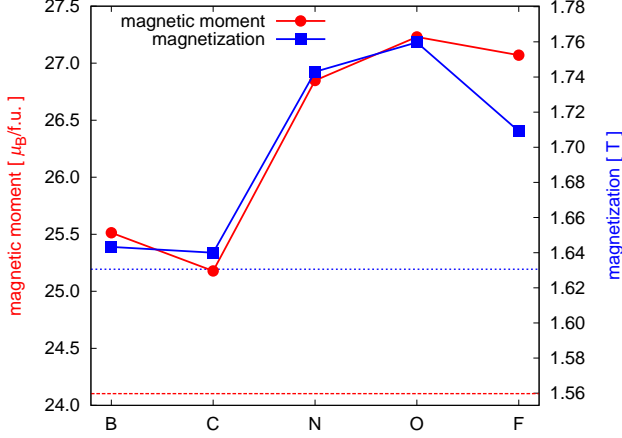


FIG. 2. (Color online) Total magnetic moment and magnetization of NdFe₁₁TiX ($X=B, C, N, O, F$) in units of $\mu_B/\text{f.u.}$ (left axis) and tesla (right axis). Theoretically optimized lattice constants and inner coordinates are used. In all the dopants, the magnetization is larger than that of NdFe₁₁Ti, 1.631 T, shown as a blue dotted line (corresponding magnetic moment is $24.10 \mu_B/\text{f.u.}$ shown as a red broken line).

Ti substitution, we use the notation of ThMn₁₂ for the structure of NdFe₁₁TiX.) Hereafter, Ti is put at the $8i$ site and X is inserted at the midpoint between Nd atoms along the c axis as shown in Fig. 1. The optimized lattice constants and fractional coordinates for NdFe₁₁Ti and NdFe₁₁TiX are shown in Tables I and II, respectively, where "empty" denotes NdFe₁₁Ti. The interstitial X expands the volume by 5% for $X=B$, 4% for C, 4% for N, 5% for O, and 7% for F.

In the present paper, we distinguish between "magnetic moment" m and "magnetization" $\mu_0 M$. "magnetic moment" is expressed in units of the Bohr magneton μ_B per atom or per formula unit, while "magnetization" is in units of Tesla which is estimated from m , volume, and the vacuum permeability μ_0 . K_1 is evaluated from the obtained $\langle r^2 \rangle A_2^0$ by using Eq. (2). We also estimate the magnetocrystalline anisotropy field $\mu_0 H_a$ ($\equiv 2\mu_0 K_1 / \mu_0 M$). The calculated magnetic properties are summarized in Table III.

The total magnetic moments are calculated to be 24.10

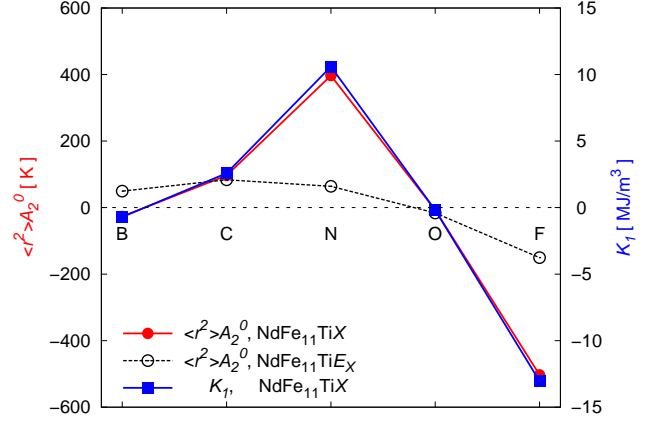


FIG. 3. (Color online) X dependence of $\langle r^2 \rangle A_2^0$ and K_1 . The filled red circles and empty black circles correspond to $\langle r^2 \rangle A_2^0$ of NdFe₁₁TiX and NdFe₁₁TiE_X, respectively. The latter is the system without X keeping the other atoms fixed at the positions of the former. The lattice constant and inner coordinate are optimized for NdFe₁₁TiX. (The parameters are shown in Tables I and II.) The structural effect shown by empty black circles is not dominant in the dopant dependence of $\langle r^2 \rangle A_2^0$. The details are discussed in Sec. IV D. In addition, K_1 is estimated from $\langle r^2 \rangle A_2^0$ by using Eq. (2), and shown as the blue squares. The red circles and blue squares do not scale exactly because of the volume effect through n_R in Eq. (2).

$\mu_B/\text{f.u.}$ for NdFe₁₁Ti and $26.84 \mu_B/\text{f.u.}$ for NdFe₁₁TiN with the structure optimization for each system. They correspond to the magnetization of 1.631 T and 1.743 T, respectively. In the previous paper, we reported the spin magnetic moment for the experimental lattice parameters.¹¹ The results were 19.99 and $20.97 \mu_B/\text{f.u.}$ for NdFe₁₁Ti and NdFe₁₁TiN, respectively. Here, the spin magnetic moments of the valence electrons other than that of the Nd- $4f$ electrons are 22.99 and $23.97 \mu_B/\text{f.u.}$ The corresponding total magnetic moments can be estimated by adding $g_J J = 3.273 \mu_B$ to these spin magnetic moment as $26.26 \mu_B/\text{f.u.}$ (1.697 T) and $27.24 \mu_B/\text{f.u.}$ (1.731 T), respectively. The nitrogenation enhances the magnetization for both optimized and experimental lattice parameters, and the increment is larger in the former case (0.112 T) than the latter (0.034 T). Experimentally, the magnetic moment is $21.273 \mu_B/\text{f.u.}$ in NdFe₁₁Ti and $23.218 \mu_B/\text{f.u.}$ in NdFe₁₁TiN_{0.5},² which correspond to 1.375 T and 1.476 T. The increment of the magnetic moment and magnetization are $3.89 \mu_B$ and 0.202 T per nitrogen, respectively. In Ref. 7, on the other hand, the magnetizations of NdFe₁₁Ti and NdFe₁₁TiN_{1.5} are reported as 1.70 T and 1.84 T, respectively; thus the magnetization difference is 0.093 T per nitrogen. These experimental results are in reasonable agreement with our calculation for the optimized lattice parameters.

Figure 2 shows the magnetic moment and magnetization for $X=B, C, N, O$, and F. The magnetic moment is

TABLE II. Optimized inner coordinates. The Nd atom is fixed at the origin. Even though the symmetry of the ThMn_{12} structure is broken by the Ti substitution, we use the notation $\text{Fe}(8f)$, $\text{Fe}(8i)$, and $\text{Fe}(8j)$ in $\text{NdFe}_{11}\text{TiX}$.

	$\text{Fe}(8f)$	$\text{Fe}(8i)$	$\text{Fe}(8j)$	X
$X=\text{B}$	(0.257, 0.252, 0.250) (0.257, 0.748, 0.750) (0.757, 0.248, 0.750) (0.757, 0.752, 0.250)	(0.374, 0.000, 0.000) (Ti) (-0.351, 0.000, 0.000) (0.007, 0.359, 0.000) (0.007, -0.359, 0.000)	(0.274, 0.500, 0.000) (-0.262, 0.500, 0.000) (0.510, 0.272, 0.000) (0.510, -0.272, 0.000)	(0.006, 0.000, 0.500)
C	(0.256, 0.252, 0.250) (0.256, 0.748, 0.750) (0.756, 0.248, 0.750) (0.756, 0.752, 0.250)	(0.374, 0.000, 0.000) (Ti) (-0.351, 0.000, 0.000) (0.007, 0.360, 0.000) (0.007, -0.360, 0.000)	(0.281, 0.500, 0.000) (-0.269, 0.500, 0.000) (0.509, 0.279, 0.000) (0.509, -0.279, 0.000)	(0.005, 0.000, 0.500)
N	(0.256, 0.252, 0.250) (0.256, 0.748, 0.750) (0.756, 0.248, 0.750) (0.756, 0.752, 0.250)	(0.373, 0.000, 0.000) (Ti) (-0.352, 0.000, 0.000) (0.006, 0.360, 0.000) (0.006, -0.360, 0.000)	(0.279, 0.500, 0.000) (-0.269, 0.500, 0.000) (0.510, 0.277, 0.000) (0.510, -0.277, 0.000)	(0.005, 0.000, 0.500)
O	(0.256, 0.251, 0.250) (0.256, 0.749, 0.750) (0.756, 0.249, 0.750) (0.756, 0.751, 0.250)	(0.373, 0.000, 0.000) (Ti) (-0.351, 0.000, 0.000) (0.006, 0.360, 0.000) (0.006, -0.360, 0.000)	(0.271, 0.500, 0.000) (-0.263, 0.500, 0.000) (0.509, 0.270, 0.000) (0.509, -0.270, 0.000)	(0.003, 0.000, 0.500)
F	(0.257, 0.251, 0.250) (0.257, 0.749, 0.750) (0.757, 0.249, 0.750) (0.757, 0.751, 0.250)	(0.373, 0.000, 0.000) (Ti) (-0.349, 0.000, 0.000) (0.006, 0.358, 0.000) (0.006, -0.358, 0.000)	(0.252, 0.500, 0.000) (-0.246, 0.500, 0.000) (0.510, 0.253, 0.000) (0.510, -0.253, 0.000)	(0.005, 0.000, 0.500)
empty	(0.254, 0.251, 0.251) (0.254, 0.749, 0.749) (0.754, 0.249, 0.751) (0.754, 0.751, 0.249)	(0.374, 0.000, 0.000) (Ti) (-0.350, 0.000, 0.000) (0.005, 0.358, 0.000) (0.005, -0.358, 0.000)	(0.269, 0.500, 0.000) (-0.264, 0.500, 0.000) (0.506, 0.274, 0.000) (0.506, -0.274, 0.000)	

TABLE III. Magnetic moment m [$\mu_{\text{B}}/\text{f.u.}$], magnetization $\mu_0 M$ [T], crystal field parameter $\langle r^2 \rangle A_2^0$ [K], magnetocrystalline anisotropy energy coefficient K_1 [MJ/m^3], and anisotropy field $\mu_0 H_a$ [T] of $\text{NdFe}_{11}\text{TiX}$ are shown for $X = \text{B}$, C, N, O, F, and $\text{NdFe}_{11}\text{Ti}$.

	m [$\mu_{\text{B}}/\text{f.u.}$]	$\mu_0 M$ [T]	$\langle r^2 \rangle A_2^0$ [K]	K_1 [MJ/m^3]	$\mu_0 H_a$ [T]
$X=\text{B}$	25.51	1.643	-27	-0.70	-1.1
C	25.18	1.640	96	2.6	4.0
N	26.84	1.743	397	10.6	15.3
O	27.23	1.760	-7	-0.2	-0.3
F	27.07	1.709	-502	-13.0	-19.2
empty	24.10	1.631	-29	-0.80	-1.2

increased by all the interstitial dopants. The corresponding magnetization is also larger than that for $\text{NdFe}_{11}\text{Ti}$ (1.631 T) but the amount of increase is partially canceled by the volume expansion. The increment of the magnetization for $X=\text{B}$ and C is small, while that for $X=\text{N}$, O, and F is significant with a jump between $X=\text{C}$ and N. Consequently, the interstitial doping of N, O, and F works positively for permanent magnets than doping of

B and C in terms of the magnetization.

We now turn to the discussion on magnetocrystalline anisotropy based on the lowest crystal field parameter A_2^0 at the Nd site. Since Nd has negative Stevens factor, positive (negative) value of A_2^0 implies uniaxial (in-plane) anisotropy. In the case of $X=\text{N}$, the interstitial doping increases the value of $\langle r^2 \rangle A_2^0$ from -29 K to 397 K. According to Eq. (2), these values correspond to $K_1 = -0.80$ MJ/m^3 and 10.6 MJ/m^3 , respectively. Thus, strong uniaxial anisotropy by nitrogenation is indicated from the calculation. The experimental anisotropy energy constant can be estimated from the magnetization and anisotropy field as $K_1 = 6.75$ MJ/m^3 in $\text{NdFe}_{11}\text{TiN}_{0.5}$ at 1.5 K² or larger than 18 MJ/m^3 in $\text{NdFe}_{11}\text{TiN}_{1.5}$ at 4.2 K⁷. If we simply assume a linear relation between dopant concentration and the increment of K_1 , our theoretical estimate is 4.9 MJ/m^3 for the former with $\text{N}_{0.5}$ and 16.3 MJ/m^3 for the latter with $\text{N}_{1.5}$.

The interstitial dopant dependence of $\langle r^2 \rangle A_2^0$ is shown in Fig. 3. $\langle r^2 \rangle A_2^0$ is -27 K for $X=\text{B}$. With increasing atomic number, $\langle r^2 \rangle A_2^0$ increases up to $X=\text{N}$, then turns to decrease, and takes a large negative value for $X=\text{F}$. Thus, the N doping is suggested to induce the strongest uniaxial anisotropy among the typical elements, B, C, N, O, and F.

IV. DISCUSSION

A. Electronic Structures

1. Fe-3d band

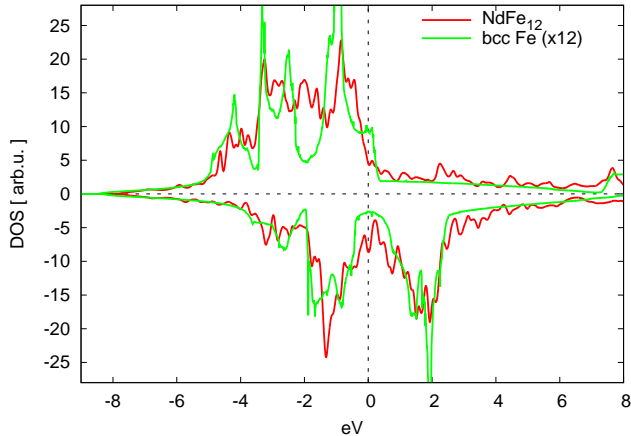


FIG. 4. (Color online) Density of states for NdFe₁₂ (red line) and bcc Fe (green line). DOS of bcc Fe has a shoulder in the majority-spin band at the Fermi level, and the width of DOS of NdFe₁₂ is narrower than that of bcc Fe. The origin of the energy is set at the Fermi level.

As our analysis of the previous paper¹¹ and the present work depends on the fact that the Fermi level lies above the majority-spin Fe-3d band, we first confirm this fact by studying the density of states (DOS). Figure 4 shows DOSs of both of NdFe₁₂ and bcc Fe. Because of the presence of a shoulder of DOS for bcc Fe at the Fermi level in the majority-spin state, the width of the majority-spin Fe-3d band looks to be slightly narrower in NdFe₁₂ than that in bcc Fe. In order to make the comparison more quantitative, we estimated the second moment of the Fe-3d band DOS with the tight-binding picture using the neighboring Fe-Fe distances and the coordination numbers. The inverse fifth power law was assumed for the interatomic distance dependence of the d - d hopping integral predicted by the canonical band picture.²⁵ We found that the second moment for NdFe₁₂ is 0.91 of that for bcc Fe being consistent with the difference in the band width mentioned above. This implies that the effective Fe-Fe distance is elongated in NdFe₁₂ compared with that in bcc Fe. The narrower d band width of NdFe₁₂ makes the majority-spin Fe-3d band virtually filled, and is expected to give larger magnetic moment. The spin moment per Fe is $2.21 \mu_B$ in NdFe₁₂ and $2.18 \mu_B$ in bcc Fe. This is consistent with the description above. However, the ratio of the spin moments $2.18/2.21 = 0.99$ is close to 1, whereas that of the second moment is 0.91. In NdFe₁₂ there is also the hybridization between Nd-5d and Fe-3d. As Nd-5d states are located above Fe-3d states, this additional

hybridization pushes down the minority-spin state more than the majority-spin state of Fe-3d and reduces the magnetic moment in NdFe₁₂, which explains such small difference in the spin moment between NdFe₁₂ and bcc Fe. The situation is not basically changed in NdFe₁₁Ti except the appearance of the split-off Ti-3d states.¹¹

2. X-2s and 2p states

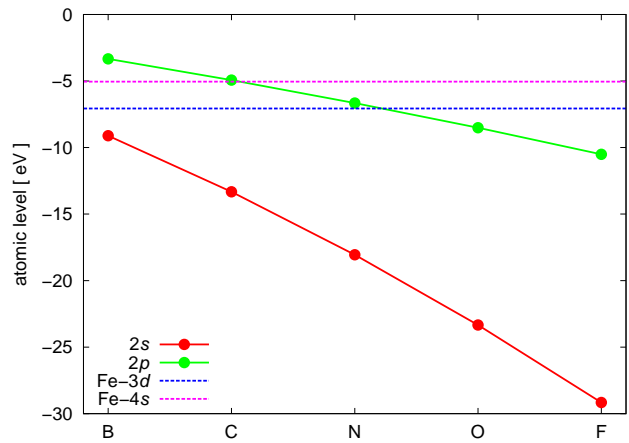


FIG. 5. (Color online) Atomic eigen levels of X-2p and -2s states are shown for $X = B, C, N, O,$ and F . Fe-3d and -4s levels are also shown. The vacuum level is taken as the origin of the vertical axis.

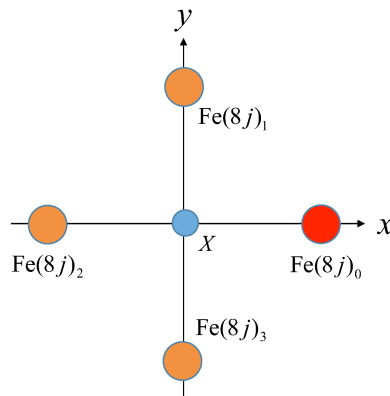


FIG. 6. (Color online) The local coordinate defined with respect to the pair between a particular X (blue circle) and a particular $Fe(8j)$ (red circle).

In order to understand the effects of the interstitial element X on magnetic properties, we have to understand the basic properties of the electronic structure associated with X , particularly X -2p states. Figure 5 shows the atomic 2s and 2p levels for each of X from B to F together with the spin-unpolarized 3d and 4s levels of Fe.

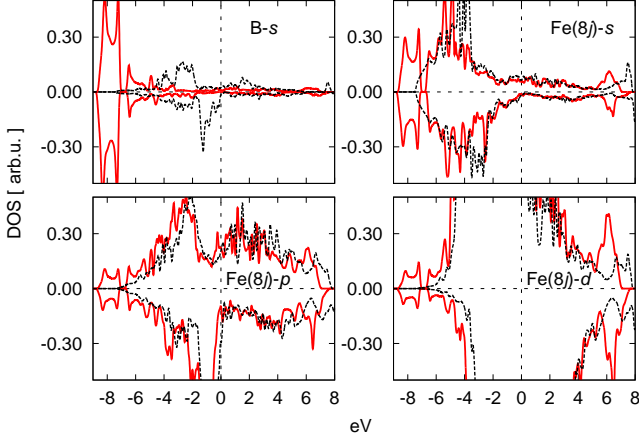


FIG. 7. (Color online) Partial density of states of $\text{NdFe}_{11}\text{TiB}$ (red solid line) and $\text{NdFe}_{11}\text{TiX}$ (black broken line). The B- s , $\text{Fe}(8j)$ - s , $-p$, $-d$ components are shown. The origin of the energy is set at the Fermi level. The split-off states can be seen around -8eV in the B- s component. Note that the weight around $+6\text{eV}$ in the $\text{Fe}(8j)$ components is not the antibonding states coupled with B- s states, but the antibonding states coupled with B- p states.

Although $2s$ levels are deeper than the Fe- $3d$ level for all X , $2p$ levels of B and C are definitely higher than the Fe- $3d$ level and the N- $2p$ level is nearly degenerate with the Fe- $3d$ level as pointed out by Kanamori.²⁶ In order to analyze the nature of the X - $2p$ states, most of the available theoretical papers take account of only the hybridization between X - $2p$ states and Fe- $3d$ states. However, it is important to take account of the Fe- $4s$, p states which form broad sp bands overlapping with the Fe- $3d$ bands in $\text{NdFe}_{11}\text{TiX}$ like in ordinary transition metals.²⁷ In the following discussion, we use the local coordinate as shown in Fig. 6. The z axis is parallel to the crystal c axis.

The B- s and $\text{Fe}(8j)$ - s , $-p$, $-d$ components of the partial DOS for $\text{NdFe}_{11}\text{TiB}$ are shown in Fig. 7. (For other X elements, see Figs. S2 and S3 of the Supplemental Material²³.) We take a projection of the eigenstates within an atomic sphere with the radius r_c . (See Fig. S1 of the Supplemental Material²³.) A split-off band at around -8eV is present in the B- s DOS and a significant weight exists also near the bottom of the band above -7eV . Such a feature is correlated with the feature existing in the s -component DOS of the $\text{Fe}(8j)$ s which are the atoms closest to X . [Note that all partial DOSs associated with $\text{Fe}(8j)$ are for four $\text{Fe}(8j)$ atoms. The local x axis is in the direction from X to each $\text{Fe}(8j)$ atom.] There is less significant weight of the p and d states of $\text{Fe}(8j)$ in the energy range of the B- $2s$ band. Therefore, the states in the split-off B- $2s$ band and near the bottom of the continuous band are dominantly formed by the hybridization between B- $2s$ and Fe- $4s$ states. It is also important to note that there is no clear evidence of the antibonding states between B- $2s$ and Fe- $4s$ states pushed up above

the Fermi level. This implies that one state is added as the occupied state for each spin state by introducing B to $\text{NdFe}_{11}\text{Ti}$. The split-off X - $2s$ band becomes deeper for higher valence elements, C to F, and the $2s$ band introduces one additional occupied state per spin for all X . This is an important result in the later discussion.

The character of the states in $\text{NdFe}_{11}\text{TiX}$ associated with the X - $2p$ states needs more careful analysis. The overall features of the partial DOS for X - $2p$ states across the typical elements X are shown in Figs. S2 and S3 in the Supplemental Material²³. For X - $2p_x$ and $2p_y$ states, both σ - and π -type hybridizations are possible with $\text{Fe}(8j)$ states. We begin the discussion with the σ -type hybridization because it is stronger. For the pair of X and $\text{Fe}(8j)_0$ located along the x direction, the $2p_x$ state of X and s , p_x , $d_{3z^2-r^2}$ and $d_{x^2-y^2}$ states of the $\text{Fe}(8j)_0$ are involved (Fig. 8). The sharp structures seen in the X - $2p_x$ DOS are reflected in the DOSs of these states of $\text{Fe}(8j)$ more or less depending on the strength of the hybridization. However, we see that the structure at the band bottom can also be seen in the DOSs of p_y and d_{xy} of $\text{Fe}(8j)$ which do not form σ -type hybridization with X - $2p_x$. Such a band bottom structure cannot be understood in terms of π -type hybridization because it is even stronger for d_{xy} than for $d_{x^2-y^2}$. The dominant mechanism of producing the structure is due to the following σ -type hybridization path; i.e., $2p_y$ at X hybridizes strongly with s of $\text{Fe}(8j)_1$ and $\text{Fe}(8j)_3$ of Fig. 6 and then these s states hybridize with p_y and d_{xy} states of $\text{Fe}(8j)_0$. On the other hand, the structures in the X - $2p_z$ component is of π -type origin and the s states at $\text{Fe}(8j)$ do not take part in the hybridization because four $\text{Fe}(8j)$ atoms and the X atom form a plane perpendicular to the crystal c axis which is taken as the z -direction. $\text{Fe}(8j)_0$ - d_{zx} states and also the $\text{Fe}(8j)_0$ - p_z state form the π -type hybridization with the X - $2p_z$ state.

From Figs. 8 and 9, one may think that the X - $2p$ components near the bottom of the host band including the split-off bands may be characterized as the X - $2p$ dominating states. However, as pointed out above, for B and C at least, the $2p$ levels are located above the Fe- $3d$ levels. Therefore, the structures near the band bottom correspond to the bonding states among X - $2p$, Fe- $3d$, and (for σ) Fe- $4s$, p states and the weight of B- $2p$ component near the band bottom is small as can be seen in Figs. 8 and 9. In this energy range, both the $\text{Fe}(8j)$ - $3d$ and $4s$ components for the σ type and only $\text{Fe}(8j)$ - $3d$ components for the π type have larger weight. As we move from B to F, the partial DOS of the X - $2p$ component shifts to a lower energy and the weight increases. The difference between σ type and π type in the energy region of the bonding states comes from the difference in the hybridization strength. The $pd\sigma$ hybridization is stronger than the $pd\pi$ hybridization by $\sqrt{3}$ in the canonical band picture²⁵ and moreover $\text{Fe}(8j)$ - $4s$ states do not contribute to the π -type hybridization.

The behavior of the antibonding states is quite different between the σ bond and the π bond. For the σ bond,

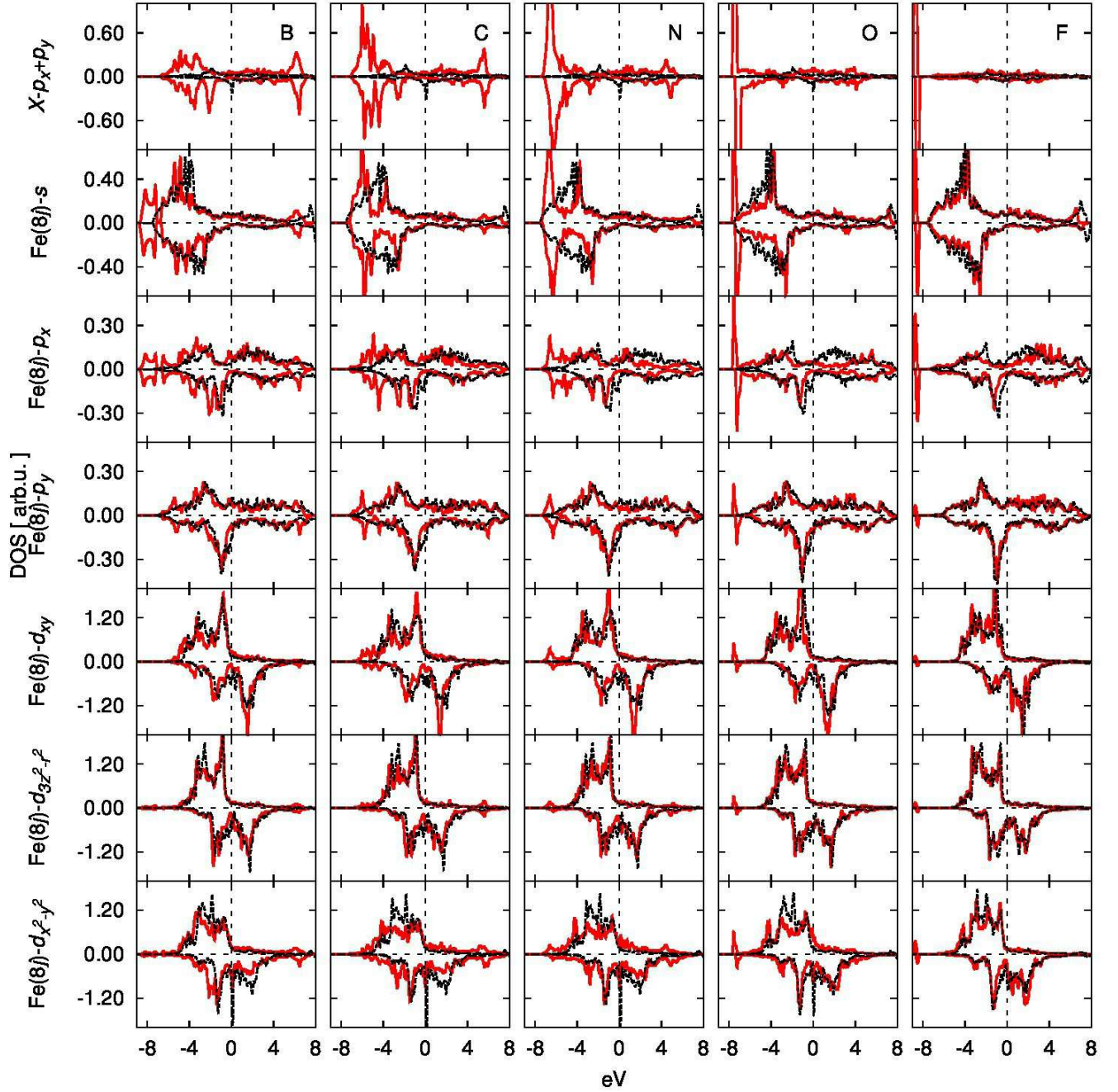


FIG. 8. (Color online) The partial DOS relating to the σ bond between X - p and $\text{Fe}(8j)$ states [X - p_x , p_y , $\text{Fe}(8j)$ - s , p_x , $d_{3z^2-r^2}$, $d_{x^2-y^2}$]. Moreover, $\text{Fe}(8j)$ - p_y and d_{xy} are also shown. The red solid lines are for $\text{NdFe}_{11}\text{TiX}$ and the black broken lines are for $\text{NdFe}_{11}\text{TiE}_X$. The origin of the energy is set at the Fermi level.

significant weight is present a bit higher than 6 eV from the Fermi level for B and this weight comes down to a lower energy for C and N. The structure becomes weak for O and nearly disappears for F. This is due to the deeper $2p$ levels and shrinking of the $2p$ wave functions for O and F. Because of the involvement of $\text{Fe}(8j)$ - $4s$ states in the σ bond, continuous spectra exist between

the sharp structures of bonding and antibonding states. For B and C, however, the weight of the continuous spectra below the Fermi level is small and only the bonding states are occupied. Moving to N and O, we see that the weight of the continuous spectra particularly in the majority-spin band increases slightly for the X - $2p_x$, $2p_y$ states even below the Fermi level. Therefore, not only

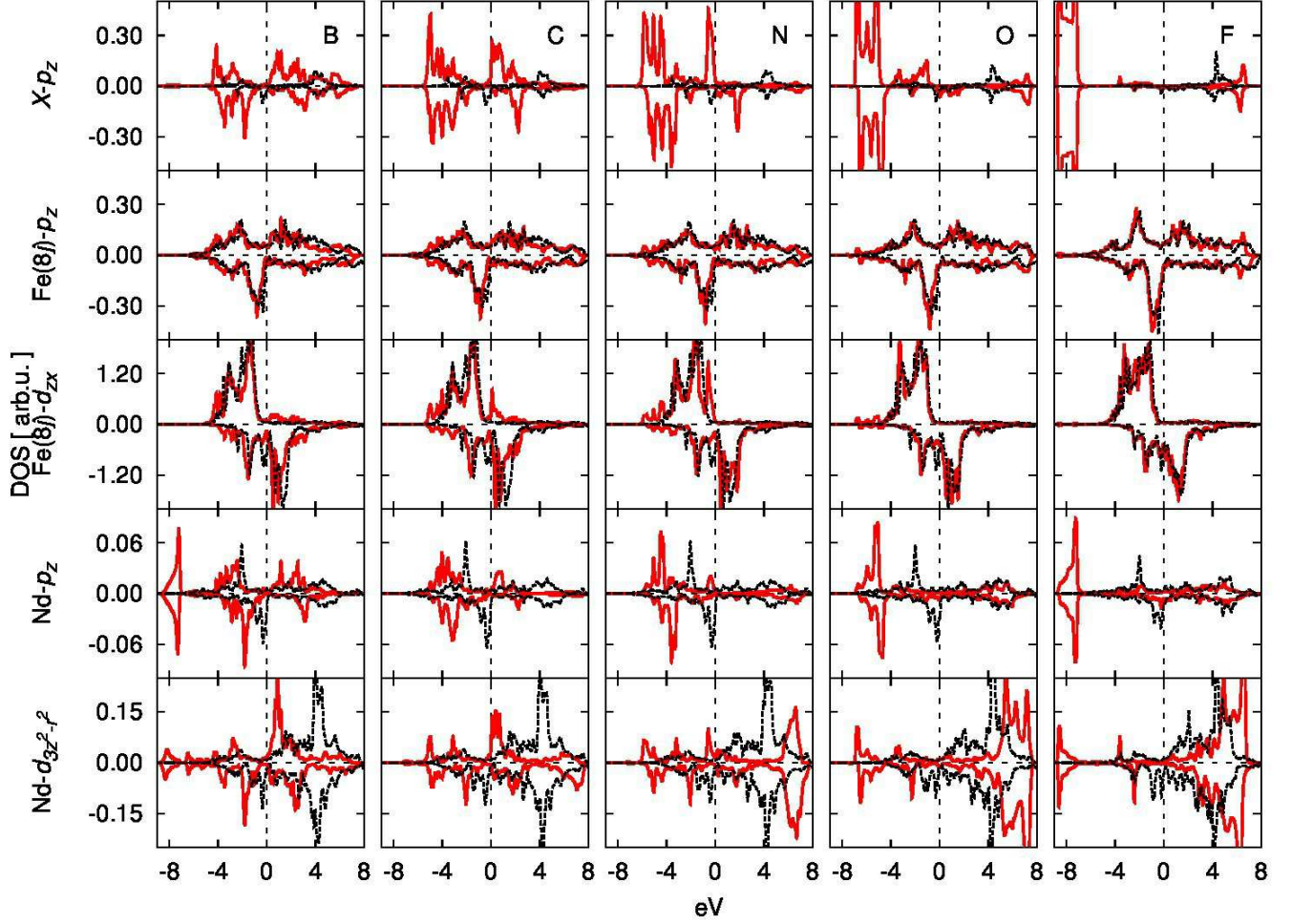


FIG. 9. (Color online) The partial DOS relating to the π bond between $X-p$ and $\text{Fe}(8j)$ states [$X-p_z$, $\text{Fe}(8j)-p_z$, d_{zx}]. $\text{Nd}-p_z$ and $d_{3z^2-r^2}$ are also shown. The red solid lines are for $\text{NdFe}_{11}\text{TiX}$ and the black broken lines are for $\text{NdFe}_{11}\text{TiEX}$. The origin of the energy is set at the Fermi level.

the bonding states but also some part of the antibonding states are occupied. The situation is different for the π bond. As $\text{Fe}(8j)-4s$ states are not involved in this case, the antibonding states are just above the Fermi level already for B, about to be occupied for C, and occupied in the majority-spin band for N. Up to N, the π antibonding state is above the Fe d band and sharp. However, for O and F, the antibonding state moves into the d band and becomes broad and small. The antibonding states start to be occupied also in the minority-spin state for O and even more occupied for F. This behavior of the antibonding π state can be clearly seen in $X-p_z$ and $\text{Fe}(8j)-d_{zx}$ in Fig. 9. Comparing these two DOSs, we find that the main component of the π antibonding state is $\text{Fe}(8j)-d_{zx}$. Traces of the antibonding π state can also be seen for $\text{Nd}-p_z$, $d_{3z^2-r^2}$ states as shown in Fig. 9. The difference between C and N in the filling of the antibonding states in the majority-spin band was pointed out before

for $R\text{Fe}_{12}X$ ²⁸ and also for $R_2\text{Fe}_{17}X_3$.^{29,30} We note that in both $R\text{Fe}_{12}X$ and $R_2\text{Fe}_{17}X_3$, X and its nearest neighbor Fe atoms form a plane perpendicular to the direction from X to R and that the s states at the Fe sites do not hybridize with the $X-2p_z$ state. Therefore, the filling of the p_π antibonding states occurs for $X=\text{N}$ in both systems.

We make brief comments on the role of Nd in the $X-2p$ related states. We find some clear structures related to the bonding and antibonding $X-2p$ states but their weight is quite small. Based on this observation, we conclude that Nd does not play an important role in the bonding with the interstitial element X and that the occupied antibonding state just below the Fermi level for N is ascribed to the hybridization between $X-2p_z$ and $\text{Fe}(8j)-3d_{zx}$ orbitals. Note, however, that the hybridization between $X-2p_z$ and $\text{Nd}-6p_z$, $5d_{3z^2-r^2}$ orbitals plays an important role in the crystal field parameter A_2^0 as

described later.

B. Optimized Structures

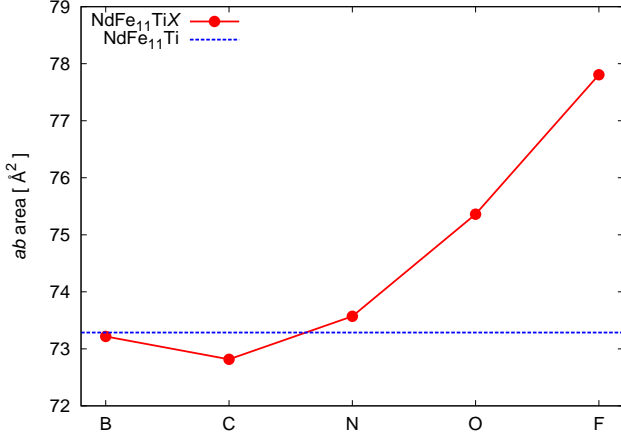


FIG. 10. (Color online) ab area of $\text{NdFe}_{11}\text{TiX}$ ($X=\text{B, C, N, O, F}$) and $\text{NdFe}_{11}\text{Ti}$.

As Table I shows, the volume expands with the interstitial X , which leads to appreciable magnetovolume effects as shown later. We also observe the following interesting aspect in Table I which reflects the bonding character related to the $X-2p$ states discussed above. Figure 10 shows the X dependence of the ab area. The broken horizontal line in this figure is the ab area for $\text{NdFe}_{11}\text{Ti}$. For $X=\text{B}$, although the volume expands by about 5 %, the ab area decreases very slightly. The ab area shrinks farther for $X=\text{C}$. Then as X moves from C to F, the ab area starts to increase. This trend is in clear contrast to the trend of the atomic radius which decreases monotonically from 0.88 Å for B to 0.58 Å for F.³¹ The behavior of the ab area of Fig. 10 reflects the strength of the covalent bond between $X-2p$ orbitals and $\text{Fe}(8j)-3d, 4s$ orbitals. As was explained in the preceding section, only their bonding states are occupied for $X=\text{B}$ and C. Therefore, the covalent bond between B or C and $\text{Fe}(8j)$ tries to keep the B, C- $\text{Fe}(8j)$ distance short. Moving from B to C, we notice that the bonding states become deeper and that the weight at C increases. These features contribute to a stronger covalent bond between C and $\text{Fe}(8j)$ because the antibonding states are still mostly unoccupied. The situations for B and C qualitatively explain the variation of the ab area in Fig. 10. On the other hand, for $X=\text{N}$, the antibonding $2p_z$ state becomes occupied in the majority-spin band. At the same time, the tail of the σ -type antibonding states are also partly occupied. Therefore the covalent bond between N and $\text{Fe}(8j)$ is weakened and the ab area becomes larger. As we move to O and F, the antibonding states will be further occupied, $2p$ levels become much deeper, and $2p$ orbitals

shrink in space. These features weaken further the $X-\text{Fe}(8j)$ covalent bond and lead to further increase of the ab area.

C. Magnetic Moment

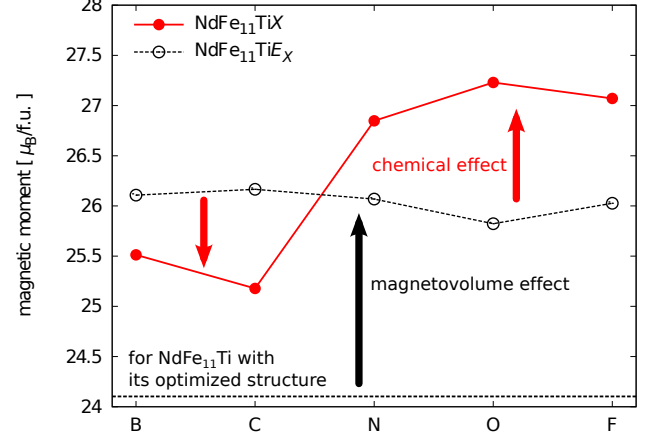


FIG. 11. (Color online) The magnetic moment per formula unit for $\text{NdFe}_{11}\text{TiX}$ ($X=\text{B, C, N, O, F}$) and $\text{NdFe}_{11}\text{Ti}$.

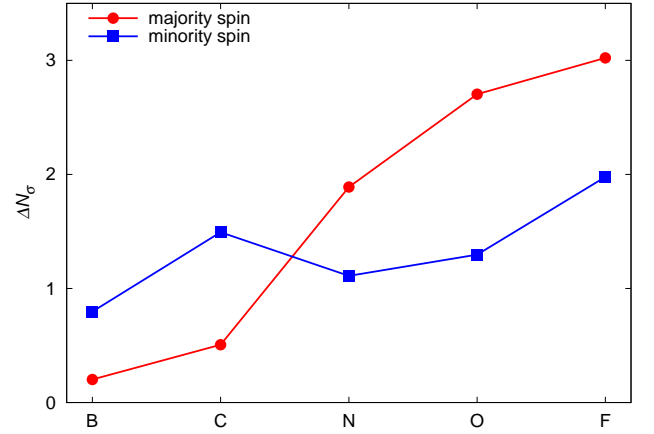


FIG. 12. (Color online) The difference of the spin-resolved number of electrons between $\text{NdFe}_{11}\text{TiX}$ and $\text{NdFe}_{11}\text{TiE}_X$. Those of the majority-spin states and minority-spin states are shown as the filled red circles and blue squares, respectively.

We show by solid circles in Fig. 11 the magnetic moment per formula unit for $\text{NdFe}_{11}\text{TiX}$ for the optimized structures. The broken line near the bottom of the figure shows the magnetic moment of $\text{NdFe}_{11}\text{Ti}$ with its optimized structure and the open circles near the middle of the figure show the magnetic moment of $\text{NdFe}_{11}\text{TiE}_X$. The change in the magnetic moment from the bottom broken line to the open circles corresponds to the magnetovolume effect, which is associated with the expanded

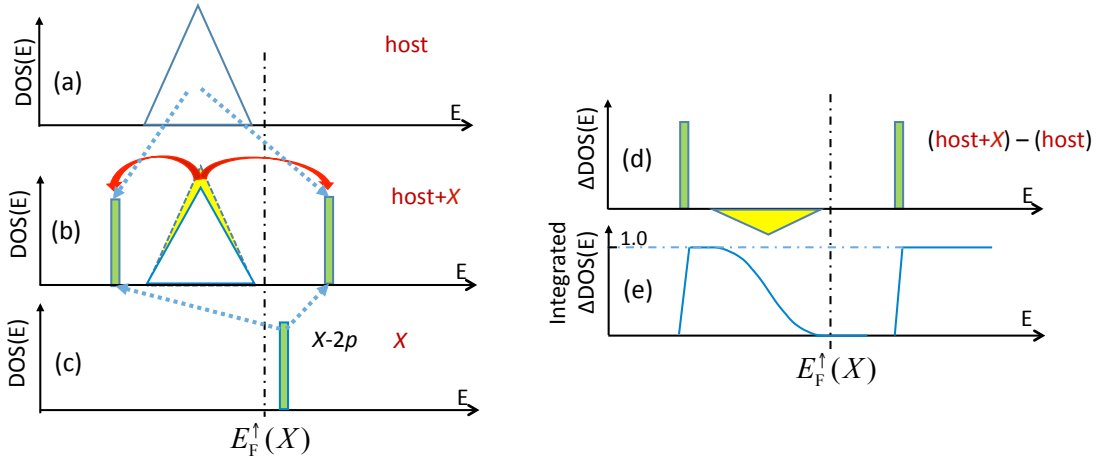


FIG. 13. (Color online) A schematic picture for explaining the behavior of $\Delta N_{\uparrow}(X)$ for $X=B$ and C .

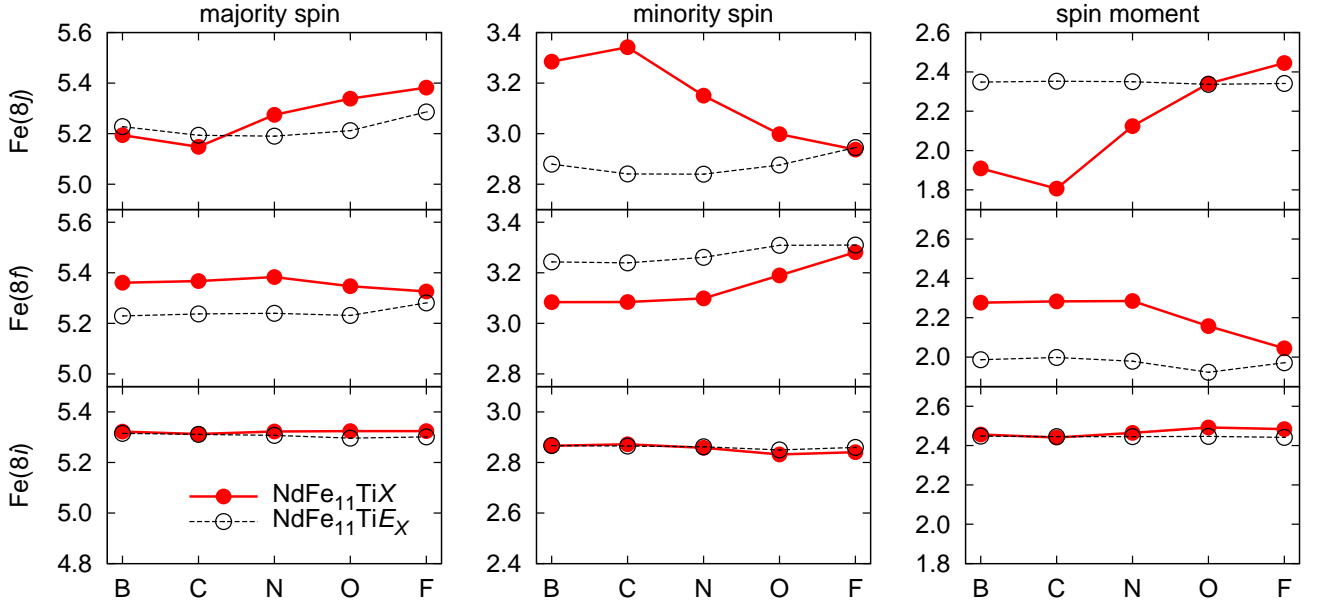


FIG. 14. (Color online) The number of local majority-spin (left) and minority-spin electrons (middle) and the spin moment (right) at Fe sites $8j$, $8f$, and $8i$ of $\text{NdFe}_{11}\text{Ti}X$ and $\text{NdFe}_{11}\text{Ti}E_X$. The integration region is given by a sphere with a radius giving the same volume of each Bader region.

volume of $\text{NdFe}_{11}\text{Ti}E_X$ compared with that of $\text{NdFe}_{11}\text{Ti}$ by 4 to 7 % depending on X . However, among the open circles, the variation in the magnetic moment does not reflect the variation in the unit cell size. On the other hand, the change in the magnetic moment from the open circles to the solid circles corresponds to the chemical effect, which is the main subject in this section. Such a magnetovolume effect and a chemical effect in materials such as Fe_4N^{32} , $\text{RFe}_{12-x}\text{M}_x\text{X}^{28,30,33,34}$, and $\text{R}_2\text{Fe}_{17}\text{X}_3^{29,30,35}$ systems were discussed before.

In order to explain the trend in the chemical effect on the magnetic moment change, we show in Fig. 12 the

change in the number of occupied states per unit cell for the spin state σ , $\Delta N_{\sigma}(X)$, caused by adding X into $\text{NdFe}_{11}\text{Ti}E_X$. In this figure and also in the following argument, we use the following convention. As already pointed out, the $2s$ states of X form split-off bands below the host valence band and introduce two additional occupied states to the host band. Therefore, we assume the valence of X , Z_X , as 1, 2, 3, 4, and 5 for B, C, N, O, and F, respectively, by focusing on only $2p$ states of X . Then $\Delta N_{\sigma}(X)$ should satisfy the charge neutrality condition given by

$$\Delta N_{\uparrow}(X) + \Delta N_{\downarrow}(X) = Z_X, \quad (4)$$

On the other hand, the chemical effect part of the magnetic moment, Δm , in Fig. 11 is given by

$$\Delta m(X) = \Delta N_{\uparrow}(X) - \Delta N_{\downarrow}(X). \quad (5)$$

There are a couple of important aspects in Fig. 12. First, $\Delta N_{\uparrow}(X)$ is quite small for $X=B$ and C . This can be understood in the following way. To simplify the situation, we tentatively neglect the presence of wide continuous $4s$, $4p$ bands above the $Fe-3d$ bands and assume that the Fermi level in the majority-spin state is located in an energy region where there are no states. Such simplification is a good approximation as long as the p_{σ} antibonding states do not make any significant contributions to the occupied states. Moreover, for the p_{π} states, the contribution from the wide $4s$, $4p$ bands is quite small. Figure 13(a) shows schematically the DOS of the host material. The Fermi level of the majority-spin state, E_F^{\uparrow} , is located just above the host band. As shown in Fig. 5, B and C have their $2p$ levels located above the $Fe-3d$ band. With introducing the hybridization between the host states and the $X-2p$ state, a bonding state appears below the host band and the antibonding state above it without being occupied. The bonding and antibonding states are formed from the original host states and the $X-2p$ state. The total number of the host states used to form the bonding and antibonding states is just one as long as the weight of the $X-2p$ state is one. Therefore, for the majority-spin state where the host band is fully occupied, while one additional state is introduced as the bonding state, the same number of states is subtracted from the host bands keeping the number of occupied states unchanged. This situation is shown in Figs. 13(d) and 13(e). Figure 13(d) shows the difference in the DOS between Fig. 13(b) and Fig. 13(a). The bonding and antibonding states are additionally introduced but some number of states whose total weight is one is subtracted from the host band. Figure 13(e) shows the integrated DOS obtained by integrating the DOS of Fig. 13(d) over energy. This quantity jumps up to unity when the upper limit of the integral crosses the bonding level, then starts to decrease as the upper limit of the integral moves into the host band region and reaches zero above the host band. It jumps up to unity again when the upper limit of the integral crosses the antibonding state. Therefore, as long as the antibonding state is unoccupied, the change in the number of occupied states per unit cell for the majority-spin state $\Delta N_{\uparrow}(X)$ is zero. At the same time, Fig. 13(e) also shows that in the minority-spin band where the Fermi level is located within the host band, $\Delta N_{\downarrow}(X) > 0$. With the above simplified model, we obtain that $\Delta N_{\uparrow}(X) = 0$ for $X = B, C$ and $\Delta N_{\downarrow}(X) = 1$ for $X=B$ and 2 for $X=C$ to satisfy Eq. (4). Accordingly, Eq. (5) gives as the chemical effect part of the magnetic moment $\Delta m(X) = -1$ for $X=B$ and -2 for $X=C$. These results are qualitatively consistent with the behavior seen in Figs. 11 and 12 for $X=B$ and C . The deviation of the results in these figures from those of the simplified model comes from the partial filling of the antibonding states

through the wide continuous $4s$ and $4p$ bands above the host band.

Second, the sudden increase in $\Delta N_{\uparrow}(X)$ from C to N is due to the filling of the antibonding p_{π} state for the majority-spin state (Fig. 9) and leads to the sudden increase in $\Delta m(X)$ in Fig. 11. Further increase of $\Delta N_{\uparrow}(X)$ from $X=N$ to F is due to the filling of p_{σ} antibonding states. Third, compared with the behavior of $\Delta N_{\uparrow}(X)$, the variation of $\Delta N_{\downarrow}(X)$ is small. This is partly due to the fact that the Fermi level of the minority-spin state is located at the deep valley in the bulk density of states. To stabilize the band energy, the Fermi level is pinned in the valley region. Another important reason for the small variation of $\Delta N(E_F^{\downarrow}, X)$ is that the Fermi level of the minority-spin state is deep inside the d band. This makes it difficult for the antibonding state to be occupied. Therefore, the minority-spin p_{π} antibonding state is filled only for $X=F$ though its weight is small due to the reduced $pd\pi$ hybridization mentioned before.

We now move to the discussion on the variation of the magnetic moment of Fe among $8j$, $8f$, and $8i$ sites, which is shown in Fig. 14. Because of the presence of Ti at one of the $8i$ sites, the electronic structure is not the same among Fe atoms even within a given category of sites. Therefore, the average value is shown for each of $8j$, $8f$, and $8i$ sites. Kanamori explained the behavior seen in Fig. 14 using the concept of *cobaltization*.²⁶ It says that by introducing B or C , the hybridization repulsion between $X-2p$ and $Fe-3d$ states pushes down the minority-spin $3d$ states of $Fe(8j)$ more strongly than its majority-spin states leading to significant increase in the minority-spin electrons. Slight decrease in the majority-spin electrons is a result of the balance between the hybridization repulsion and the local charge neutrality requirement in metals, with the $Fe(8j)$ being slightly more electron populated. The resulting electronic structure of $Fe(8j)$ is similar to that of Co and the magnetic moment of $Fe(8j)$ is reduced by about $0.4 \mu_B$. On the other hand, the change in the electronic structure at $Fe(8f)$ is just opposite to that at $Fe(8j)$. Kanamori also pointed out that the behavior at $Fe(8f)$ can be explained in parallel with the change at the Fe sites next to Co in the $Fe-Co$ alloy. The above picture of *cobaltization* caused by the interstitial B is schematically explained by Figs. 1 and 2 in one of his papers.³⁶ The concept of *cobaltization* seems to be reasonable for $X=B$ and C . However, the net magnetic moment is decreased by the chemical effect, and the enhancement by X is due to the magnetovolume effect. For $X=N, O$, and F , the atomic $2p$ level is very close to or below the $Fe-3d$ level (Fig. 5) and the picture of *cobaltization* is not applicable. The positive chemical effect for these elements is due mainly to coming down of the p_{π} antibonding state below the Fermi level in the majority-spin state.

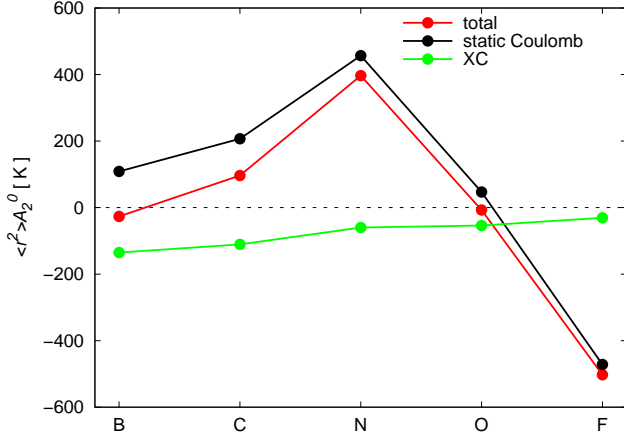


FIG. 15. (Color online) $\langle r^2 \rangle A_2^0$ of NdFe₁₁TiX. Contributions from the static Coulomb and the exchange-correlation potential are shown by black circles and green circles, respectively. Red circles show the sum of the two contributions.

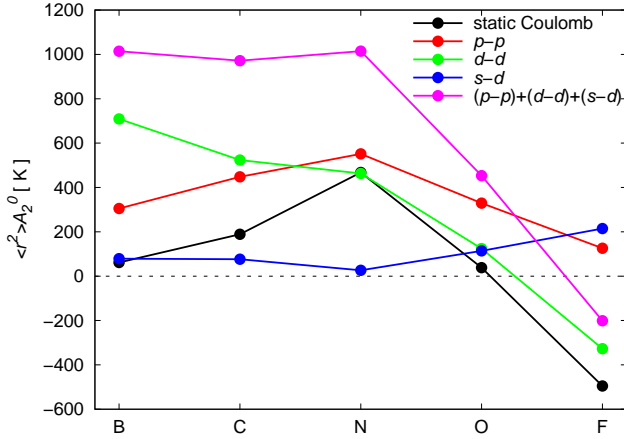


FIG. 16. (Color online) p - p , d - d , and s - d components in $\langle r^2 \rangle A_2^0$. The cutoff radii are determined from Bader analysis.

D. Crystal field parameter

Finally, we discuss the origin of the dopant dependence in $\langle r^2 \rangle A_2^0$. In order to see whether the dopant dependence can be explained from the structure change, we plot $\langle r^2 \rangle A_2^0$ of NdFe₁₁TiX in Fig. 3 by open circles. The difference among $X=B, C, N, O$, and F is within about 220 K and the structural effect is not sufficient to explain the dopant dependence.

The potential used in $\langle r^2 \rangle A_2^0$ [Eq. (3)] consists of the static Coulomb (Hartree) and the exchange-correlation potentials. Figure 15 shows the dopant dependence of each contribution. We can see that the static Coulomb potential dominantly affects the dopant dependence of $\langle r^2 \rangle A_2^0$. In the succeeding analysis, we concentrate on

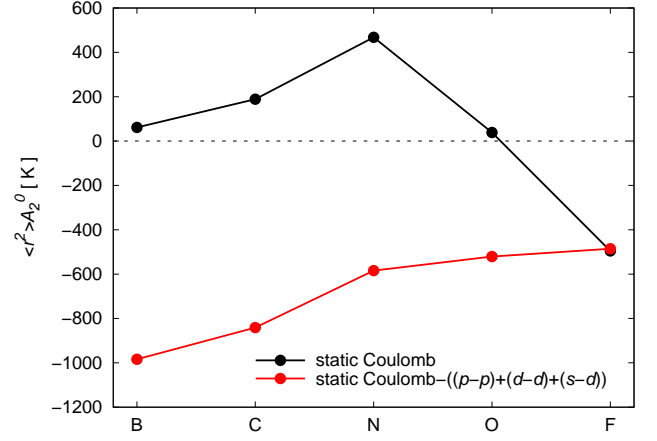


FIG. 17. (Color online) Static Coulomb contribution to $\langle r^2 \rangle A_2^0$ brought by the off-site charge density (outside the Nd site).

the contribution from the static Coulomb potential.

The static Coulomb potential is caused by the charge density. We separate it into the on-site charge (at the Nd site) and off-site charge. Since the Nd-ion charge is spherically symmetric, the on-site contribution to $\langle r^2 \rangle A_2^0$ is a consequence of the aspherical (e.g., p , d) component of the electron density at the Nd-site. To see this in more detail, we decompose the electron density within the Bader sphere at the Nd-site into the components having $Y_{lm}^* Y_{l'm'}$ as follows³⁷.

$$V_H(\mathbf{r}) = - \int_{R < R_c} d^3 R \frac{\rho(\mathbf{R})}{|\mathbf{r} - \mathbf{R}|} \quad (6)$$

$$\rho(\mathbf{R}) = - \sum_i^{\text{occ}} \left| \sum_l \sum_{m=-l}^m f_{lm}^i(R) Y_{lm}(\hat{\mathbf{R}}) \right|^2 \quad (7)$$

$$= - \sum_{lm'l'm'} n_{e,lm'l'm'}(R) Y_{lm}(\hat{\mathbf{R}})^* Y_{l'm'}(\hat{\mathbf{R}}) \quad (8)$$

where,

$$n_{e,lm'l'm'}(R) \equiv \sum_i^{\text{occ}} f_{lm}^i(R)^* f_{l'm'}^i(R) \quad (9)$$

$f_{lm}^i(R)$ is the radial part of the lm component in the i th eigenstate. The cutoff radius R_c of the integration in Eq. (6) is determined from the Bader region mentioned above ($=r_c$). [We note that R_c is conceptually different from r_c , although the same value is taken in the actual calculations. The former is the cutoff radius of the charge density to evaluate the static Coulomb potential, whereas the latter is the cutoff radius for the potential in Eq.(3).] $1/|\mathbf{r} - \mathbf{R}|$ can be expanded by the real spherical harmonics:

$$\frac{1}{|\mathbf{r} - \mathbf{R}|} = \sum_{lm} \frac{4\pi}{2l+1} \frac{r_{<}^l}{r_{>}^{l+1}} Z_l^m(\hat{\mathbf{r}}) Z_l^m(\hat{\mathbf{R}}) \quad (10)$$

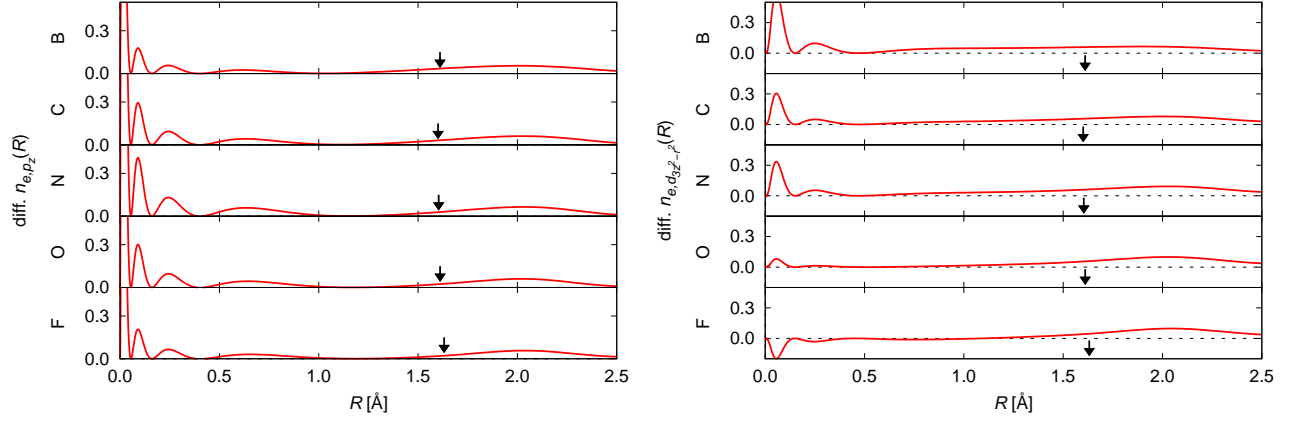


FIG. 18. (Color online) p_z and $d_{3z^2-r^2}$ components ($n_{e,p_z} \equiv n_{e,1010}$ and $n_{e,d_{3z^2-r^2}} \equiv n_{e,2020}$) of the electron density difference between $\text{NdFe}_{11}\text{TiX}$ and $\text{NdFe}_{11}\text{TiE}_X$ are shown on the left and right panels, respectively. The horizontal axis is the distance from Nd. The positive value means that $n_{e,lm'l'm'}$ is increased by introducing X. The black arrows indicate the Bader radius.

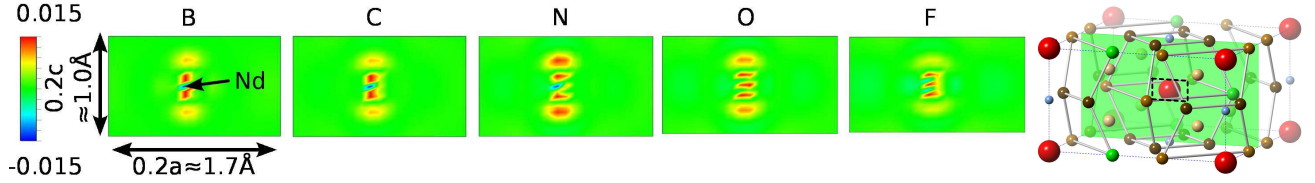


FIG. 19. (Color online) Electron density difference between $\text{NdFe}_{11}\text{TiX}$ and $\text{NdFe}_{11}\text{TiE}_X$. The density increases (decreases) in the red (blue) region. The figures show the density difference map on the ac plane around the Nd atom. The Nd atom is at the center of each figure. The vertical and horizontal ranges are 0.2 times c and a axis, respectively. The displayed region is indicated by a black dashed box on the right panel. The outermost red island corresponds to the peak at 0.25\AA in Fig. 18.

Here, $r_{<} \equiv \min(r, R)$ and $r_{>} \equiv \max(r, R)$. Inserting Eqs.(8), (9), and (10) into Eq.(6), and performing angular integration of $Z_l^m(\hat{\mathbf{R}})Y_{l'}^{m'}(\hat{\mathbf{R}})^*Y_{l''}^{m''}(\hat{\mathbf{R}})$, three components, $\sum_{m=-1}^1 n_{e,1m1m}$, $\sum_{m=-2}^2 n_{e,2m2m}$, and $n_{e,0020} + n_{e,2000}$, yield nonzero contribution to A_2^0 . The dopant dependencies of the three components, p - p ($\equiv \sum_{m=-1}^1 n_{e,1m1m}$), d - d ($\equiv \sum_{m=-2}^2 n_{e,2m2m}$), and s - d ($\equiv n_{e,0020} + n_{e,2000}$), are shown in Fig. 16. Among the three, the p - p electron density gives a peak structure at $X=\text{N}$, which is similar to the behavior of the total $\langle r^2 \rangle A_2^0$. In contrast, the contribution from d - d density decreases monotonically from $X=\text{B}$ to F . The s - d cross-term contribution is small compared with the p - p and d - d contributions. We also plot the remaining component defined as the static Coulomb minus the contribution from the electron density within the Bader atomic sphere in Fig. 17. The contribution increases monotonically as the dopant changes from B to F.

In order to understand the dopant dependence of the p - p and d - d components, we decompose them into each m component, and compare the results for $\text{NdFe}_{11}\text{TiX}$ and for $\text{NdFe}_{11}\text{TiE}_X$. We found that most of the components are not changed between $\text{NdFe}_{11}\text{TiX}$ and $\text{NdFe}_{11}\text{TiE}_X$. However, the p_z and $d_{3z^2-r^2}$ components are significantly changed as shown in Fig. 18, where the $n_{e,lm'l'm'}(R)$ differences for p_z and $d_{3z^2-r^2}$ are plotted as a function of

the distance R from Nd. The changes are prominent in the vicinity of the Nd atom within a 0.5\AA radius. In Fig. 19, the density difference map on the ac plane including the Nd atom is shown. Both p_z and $d_{3z^2-r^2}$ orbitals have an anisotropic shape expanding along the c axis. Correspondingly, an increase in the density difference is observed above and below the Nd site along the c axis. This accumulated electron charge suppresses the aspherical $4f$ -electron density from above and below the Nd site, which induces the uniaxial anisotropy. For p_z density, the difference increases from $X=\text{B}$ to N and decreases from N to F , and for $d_{3z^2-r^2}$, it decreases monotonically from $X=\text{B}$ to F . These density differences near the Nd site explain the dopant dependence of the p - and d -components. The influence of the bonding charge between X and R has also been discussed in Ref. 30.

There still remains the contribution in the static Coulomb potential other than the contribution from the electron density within the Bader atomic sphere. This can be interpreted as the off-site contribution, namely the contribution from the charges outside the Nd-atomic sphere with R_c . The increasing behavior of this contribution shown in Fig. 17 reflects the electronegativity of the interstitial dopants. The dopant elements B, C, N, O, and F have the electronegativity 2.04, 2.55, 3.04, 3.44, 3.98, respectively.³⁸ F tends to attract the negative charge more than B. The attracted negative charge at

the X site gives the Coulomb repulsive interaction at the Nd site along the c axis. This contribution for $\langle r^2 \rangle A_2^0$ has a positive value. Thus, F gives a less negative value than B.

These three contributions, p - p , d - d electron charges at Nd-site, and the charge at the interstitial dopant, explain the nonmonotonic dopant dependence of $\langle r^2 \rangle A_2^0$.

V. CONCLUSION

We have studied the magnetic properties of $\text{NdFe}_{11}\text{TiX}$ with $X=\text{B, C, N, O, and F}$ with first-principles electronic structure calculations to find a better interstitial dopant for a permanent magnet. According to our study, the total magnetic moment is increased by doping B, C, N, O, and F at the interstitial site. The magnetic moment increase can be separated into the magnetovolume effect and the chemical effect, the latter of which depends strongly on the dopant. The chemical effect is negative for B and C and becomes suddenly positive for N, O, and F. By studying carefully the basic electronic structures of $\text{NdFe}_{11}\text{TiX}$ from the viewpoint of the hybridization between X and $\text{Fe}(8j)$, we gave an explanation to the mechanism of the negative chemical effect for B and C. The sudden increase in the chemical effect part of the magnetic moment from C to N is due to the coming down below the Fermi level of the majority-spin p_π antibonding state formed between

X and $\text{Fe}(8j)$.

The results for $\langle r^2 \rangle A_2^0$ suggest that the strongest enhancement of uniaxial anisotropy is achieved by $X=\text{N}$. We analyzed the dopant dependence of $\langle r^2 \rangle A_2^0$ from the decomposed electron density $n_{e,lm'l'm'}(R)$. The analysis suggests that the bonding charge between Nd and X , and the charge at the X site can explain the increasing trend from B to N and decreasing trend from N to F of the magnetocrystalline anisotropy.

The present study suggests that the interstitial nitrogenation is the most appropriate among the typical elements B, C, N, O, and F doping in terms of the magnetization and magnetocrystalline anisotropy.

ACKNOWLEDGMENTS

The authors would like to thank Prof. H. Akai and Dr. S. Hirose for fruitful discussions. This work was supported by the Elements Strategy Initiative Project under the auspices of MEXT, MEXT HPCI Strategic Programs for Innovative Research (SPIRE) and Computational Materials Science Initiative (CMSI). The computations have been partly carried out using the facilities of the Supercomputer Center, the Institute for Solid State Physics, the University of Tokyo, and the supercomputer of ACCMS, Kyoto University, and also by the K computer provided by the RIKEN Advanced Institute for Computational Science (Project ID:hp140150).

-
- ¹ S. Hirose, Y. Matsuura, H. Yamamoto, S. Fujimura, M. Sagawa, and H. Yamauchi, *J. Appl. Phys.* **59**, 873 (1986).
 - ² Y. C. Yang, X. D. Zhang, L. S. Kong, Q. Pan, and S. L. Ge, *Solid State Commun.* **78**, 317 (1991).
 - ³ Y. C. Yang, X. D. Zhang, S. L. Ge, Q. Pan, L. S. Kong, H. Li, J. L. Yang, B. S. Zhang, Y. F. Ding, and C. T. Ye, *J. Appl. Phys.* **70**, 6001 (1991).
 - ⁴ D. B. D. Mooij and K. H. J. Buschow, *J. Less-Common Met.* **136**, 207 (1988).
 - ⁵ K. H. J. Buschow, *J. Magn. Magn. Mater.* **100**, 79 (1991).
 - ⁶ R. Verhoef, F. R. de Boer, Z. Zhi-dong, and K. H. J. Buschow, *J. Magn. Magn. Mater.* **75**, 319 (1988).
 - ⁷ M. Akayama, H. Fujii, K. Yamamoto, and K. Tatami, *J. Magn. Magn. Mater.* **130**, 99 (1994).
 - ⁸ D. P. F. Hurley and J. M. D. Coey, *J. Phys.: Condens. Matter* **4**, 5573 (1992).
 - ⁹ Z. W. Li, X. Z. Zhou, and A. H. Morrish, *J. Phys.: Condens. Matter* **5**, 3027 (1993).
 - ¹⁰ J. Yang, P. Oleinek, D. Eckert, M. Wolf, and K.-H. Müller, *J. Magn. Magn. Mater.* **214**, 44 (2000).
 - ¹¹ T. Miyake, K. Terakura, Y. Harashima, H. Kino, and S. Ishibashi, *J. Phys. Soc. Jpn.* **83**, 043702 (2014).
 - ¹² Y. Harashima, K. Terakura, H. Kino, S. Ishibashi, and T. Miyake, *JPS Conf. Proc.* **5**, 011021 (2015).
 - ¹³ Y. Hirayama, Y. K. Takahashi, S. Hirose, and K. Hono, *Scripta Materialia* **95**, 70 (2015).
 - ¹⁴ <http://qmas.jp/>.
 - ¹⁵ P. Hohenberg and W. Kohn, *Phys. Rev.* **136**, B864 (1964).
 - ¹⁶ W. Kohn and L. J. Sham, *Phys. Rev.* **140**, A1133 (1965).
 - ¹⁷ P. E. Blöchl, *Phys. Rev. B* **50**, 17953 (1994).
 - ¹⁸ G. Kresse and D. Joubert, *Phys. Rev. B* **59**, 1758 (1999).
 - ¹⁹ J. P. Perdew, K. Burke, and M. Ernzerhof, *Phys. Rev. Lett.* **77**, 3865 (1996).
 - ²⁰ M. Richter, P. M. Oppeneer, H. Eschrig, and B. Johansson, *Phys. Rev. B* **46**, 13919 (1992).
 - ²¹ R. F. W. Bader, *Atoms in Molecules: A Quantum Theory* (Oxford University Press, Oxford, 1990).
 - ²² G. Henkelman, A. Arnaldsson, and H. Jónsson, *Comput. Mater. Sci.* **36**, 354 (2006).
 - ²³ For the data of the Bader radius, the partial density of states at X , $\text{Fe}(8j)$, and Nd sites, and the number of majority and minority spin electrons at X site.
 - ²⁴ O. Moze, R. M. Ibberson, and K. H. J. Buschow, *Solid State Commun.* **78**, 473 (1991).
 - ²⁵ O. K. Andersen, *Phys. Rev. B* **12**, 3060 (1975).
 - ²⁶ J. Kanamori, *Prog. Theor. Phys. Suppl.* **101**, 1 (1990).
 - ²⁷ K. Terakura, *J. Phys. F* **7**, 1773 (1977).
 - ²⁸ S. Asano, S. Ishida, and S. Fujii, *Physica B* **190**, 155 (1993).
 - ²⁹ L. Steinbeck, M. Richter, U. Nitzsche, and H. Eschrig, *Phys. Rev. B* **53**, 7111 (1996).
 - ³⁰ S. Asano and M. Yamaguchi, *Physica B* **237–238**, 541 (1997).
 - ³¹ P. Pykkö, *Phys. Rev. B* **85**, 024115 (2012).
 - ³² H. Akai, M. Takeda, M. Takahashi, and J. Kanamori,

- Solid State Commun. **94**, 509 (1995).
- ³³ A. Sakuma, J. Phys. Soc. Jpn. **61**, 4119 (1992).
- ³⁴ J. Yang, W. Mao, Y. Yang, S. Ge, and D. Chen, Phys. Rev. B **56**, 15647 (1997).
- ³⁵ P. Uebele, K. Hummler, and M. Föhnle, Phys. Rev. B **53**, 3296 (1996).
- ³⁶ M. Ogura, H. Akai, and J. Kanamori, J. Phys. Soc. Jpn. **80**, 104711 (2011).
- ³⁷ R. Coehoorn, K. H. J. Buschow, M. W. Dirken, and R. C. Thiel, Phys. Rev. B **42**, 4645 (1990).
- ³⁸ A. Allred, J. Inorg. and Nucl. Chem. **17**, 215 (1961).

VI. SUPPLEMENTAL MATERIAL

In this Supplemental Material, we show the following figures.

1. Fig. S1: The radius of the atomic sphere whose volume is that of the Bader region^{21,22} for each atom in the unit cell of $\text{NdFe}_{11}\text{TiX}$. The same atomic sphere radius is used for $\text{NdFe}_{11}\text{TiE}_X$.
2. Fig. S2: The partial DOS of X in $\text{NdFe}_{11}\text{TiX}$.
3. Fig. S3: The zoomed figures of Fig. S2.
4. Fig. S4: The partial DOS of $\text{Fe}(8j)$ in $\text{NdFe}_{11}\text{TiX}$.
5. Fig. S5: The partial DOS of Nd in $\text{NdFe}_{11}\text{TiX}$.
6. Fig. S6: The number of electrons for each spin state in the atomic sphere for each X in $\text{NdFe}_{11}\text{TiX}$.

The partial DOSs in Figs. S2, S3, S4 and S5 and the number of electrons in Fig. S6 are given for the atomic sphere with the radius given in Fig. S1. X - s and $p_x + p_y$ components in Figs. S2 and S2 are related with the σ bond between X and $\text{Fe}(8j)$, while X - p_z component is related with the π bond. In Fig. S6, the X - p_z component shows a jump from $X=\text{C}$ to N. This is due to the occupation of the anti-bonding states at $X=\text{N}$.

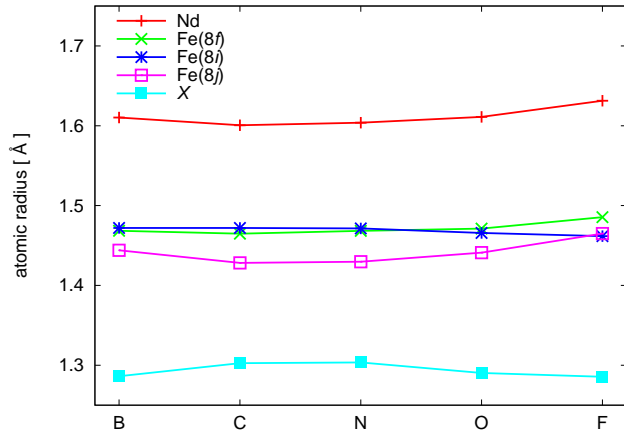


FIG. S1. (Color online) The sphere radius used for the integration region of the partial DOS for each X .

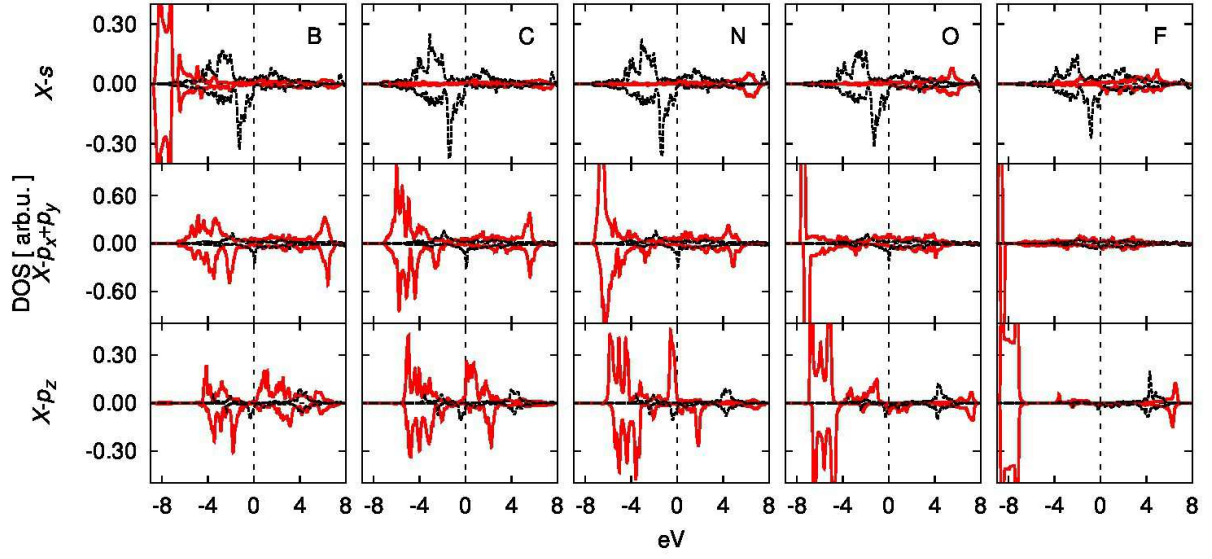


FIG. S2. (Color online) Partial density of states at X of $\text{NdFe}_{11}\text{TiX}$. The s components (upper panel), the sumation of p_x and p_y components (middle panel), and p_z components (lower panel) are shown.

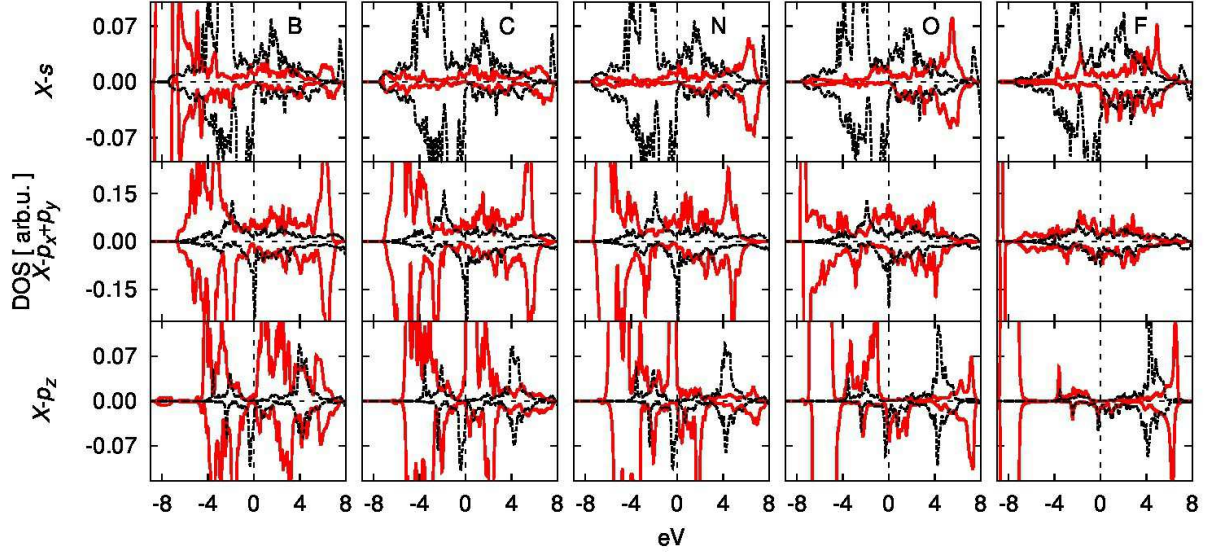


FIG. S3. (Color online) Zoomed figures for partial density of states at X of $\text{NdFe}_{11}\text{TiX}$ corresponding to Fig. S2.

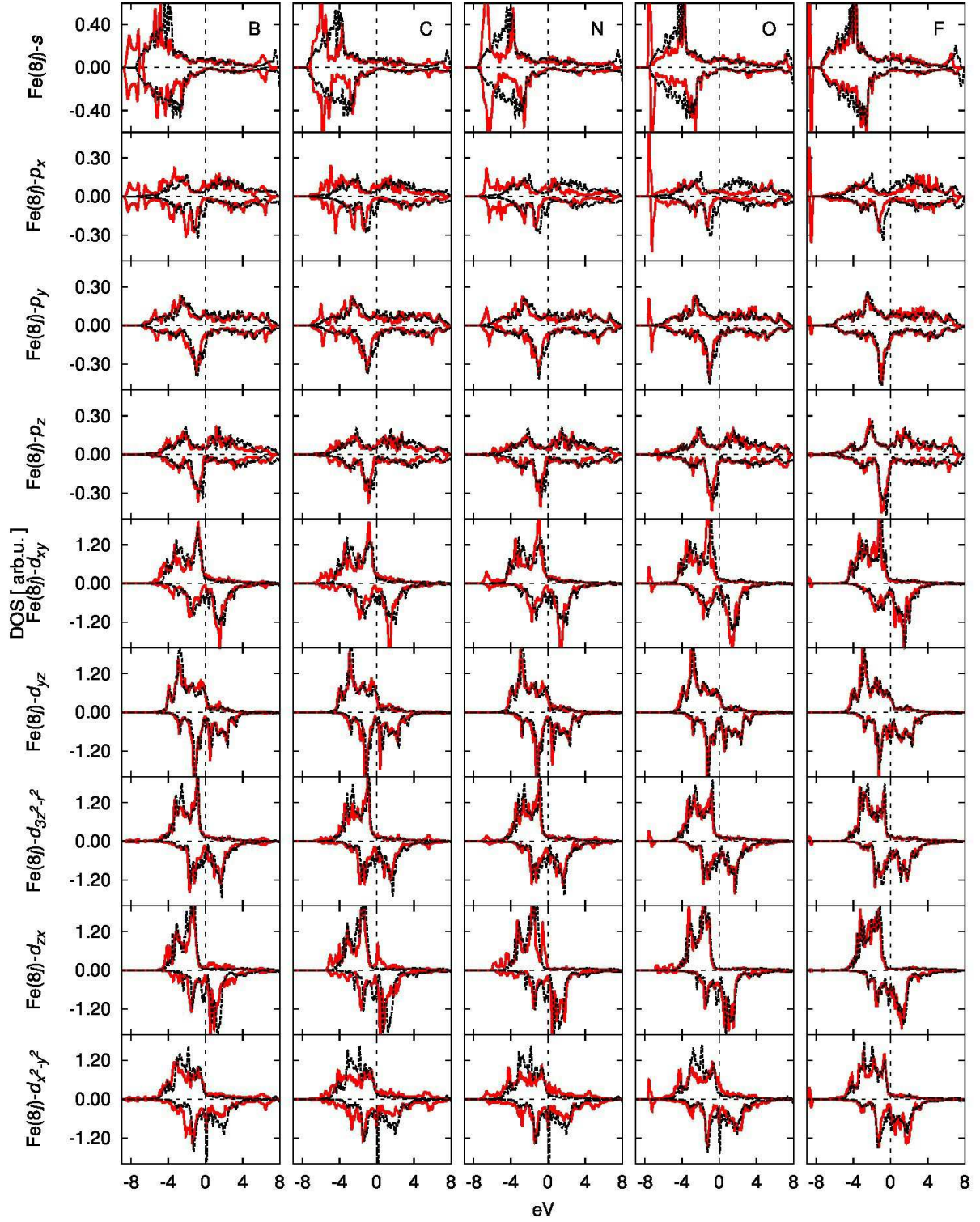


FIG. S4. (Color online) Partial density of states at Fe(8j) of NdFe₁₁TiX. The s , p_x , p_y , p_z , d_{xy} , d_{yz} , $d_{3z^2-r^2}$, d_{zx} , $d_{x^2-y^2}$ components are shown. The red solid lines for NdFe₁₁TiX and the black broken lines for NdFe₁₁TiE_X.

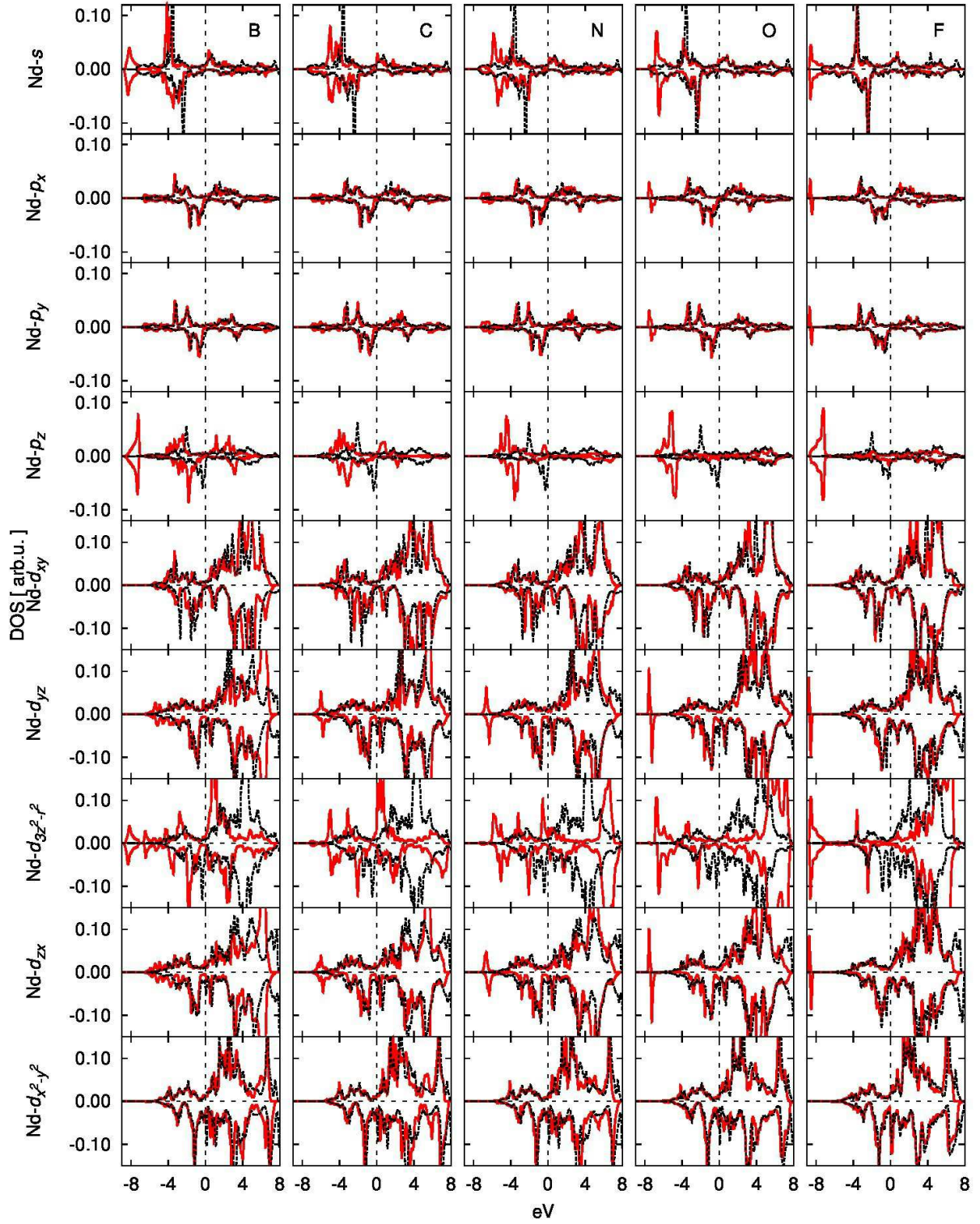


FIG. S5. (Color online) Partial density of states at Nd of NdFe₁₁TiX. The s , p_x , p_y , p_z , d_{xy} , d_{yz} , $d_{3z^2-r^2}$, d_{zx} , $d_{x^2-y^2}$ components are shown. The red solid lines for NdFe₁₁TiX and the black broken lines for NdFe₁₁TiE_X.

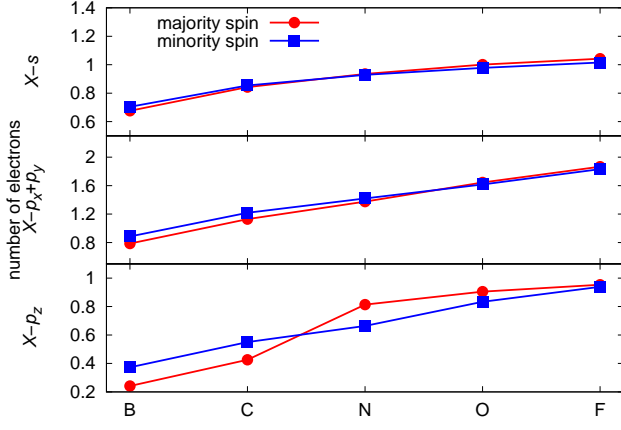


FIG. S6. (Color online) The number of majority spin and that of minority spin electrons within the sphere around X . The components are separated into each orbitals, s , $p_x + p_y$, and p_z .